ELSEVIER

Applied Surface Science 178 (2001) 105–115

applied surface science

www.elsevier.nl/locate/apsusc

Chemical mapping of elemental sulfur on pyrite and arsenopyrite surfaces using near-infrared Raman imaging microscopy

Molly M. McGuire[a], Karim N. Jallad[b], Dor Ben-Amotz[b], Robert J. Hamers[a,*]

[a]*Department of Chemistry, University of Wisconsin–Madison, 1101 University Avenue, Madison, WI 53706, USA*
[b]*Department of Chemistry, Purdue University, 1393 Brown Building, West Lafayette, IN 47907, USA*

Received 25 January 2001; accepted 29 March 2001

Abstract

Near-infrared Raman imaging microscopy (NIRIM) was used to produce chemical images of the distribution of elemental sulfur on oxidized pyrite and arsenopyrite surfaces. Analysis using Savitsky–Golay filtering permits an unambiguous identification of surface products even in the presence of broad background signals. Rather than forming a continuous, passivating layer at the mineral surface, the NIRIM images reveal that elemental sulfur forms in isolated patches on the order of tens of microns in diameter. The potential implications of this strongly heterogeneous distribution of chemical products for geochemical modeling of acid mine drainage (AMD) are discussed.

PACS: 82.80.-d; 68.35.DV; 91.65.V

Keywords: Raman imaging; Sulfide surfaces; Elemental sulfur

1. Introduction

Geochemical transformations often produce spatially heterogeneous distributions of surface products due to the inherent inhomogeneities, such as dislocations and inclusions, in natural mineral samples. These inhomogeneities can locally modify the chemical reactivity of the mineral and create areas of preferential reaction. The spatial distribution of products can provide important clues about reaction mechanisms and ultimately lead to better predictive models. For example, understanding whether reaction products are distributed homogeneously or inhomogeneously on a surface may provide clues as to possible rate limiting steps of a surface reaction.

The oxidative dissolution of sulfide minerals and the subsequent problem of acid mine drainage (AMD) is one such geochemical system. Pyrite, FeS_2, the most abundant of the sulfide minerals, has been studied extensively and several comprehensive reviews of the literature have been assembled [1–5]. Previous studies have established that ferric iron, Fe^{3+}, is a much more efficient oxidizer than dissolved oxygen [6,7], and the regeneration of ferric iron from ferrous iron is the rate-limiting step at low pH [8]. Despite the advances made in understanding the kinetics and mechanism of pyrite dissolution, many of the details of the reaction have not been drawn out. In particular, the distribution of sulfur-containing reaction products is not well understood. According to a proposed

* Corresponding author. Tel.: +1-608-262-6371; fax: +1-608-262-0453.
E-mail address: rjhamers@facstaff.wisc.edu (R.J. Hamers).

0169-4332/01/$ – see front matter
PII: S0169-4332(01)00303-8

mechanism for the dissolution of pyrite, the primary sulfur product released to solution is thiosulfate [7,9]. This mechanism, however, does not explain the formation of elemental sulfur (S_8), which has been observed on the mineral surface during the oxidative dissolution of pyrite [10–15]. Spatially resolved maps of the chemical speciation of the mineral surface could help resolve the details of the formation of the sulfur reaction products and the influence these products may have on subsequent surface reactions.

Several previous studies have demonstrated that sulfur-vacancy defect sites exposed at pyrite surfaces exhibit unusually high reactivity for the adsorption of gas-phase reactants [16,17], as well as the oxidation of pyrite in H_2O and H_2O/O_2 environments [18]. Additionally, scanning tunneling microscopy (STM) studies of pyrite have suggested that step edges may provide sites of enhanced redox reactivity [19], while the growth of oxide patches on air-oxidized samples is influenced by specific crystallographic directions [20] and is initially localized by surface sites of higher reactivity [21]. As demonstrated in these previous studies, natural samples contain various sources of structural and chemical heterogeneity that play a role in the reactivity of the mineral surface. By obtaining chemical maps of the reaction products, it is possible to glean new insights into the effects these heterogeneities may have on the speciation and spatial distribution of sulfur reaction products after oxidation by ferric iron.

While chemical and spatial information can be obtained from techniques such as scanning electron microscopy (SEM) with energy-dispersive X-ray analysis (EDX) and imaging X-ray photoelectron spectroscopy (XPS), these techniques require the use of high-energy excitation sources (electrons and X-rays, respectively), which can hasten evaporative loss of elemental sulfur under vacuum [22]. Additionally, since sulfide minerals contain sulfur, distinguishing sulfur reaction products at the surface from the sulfide present in the bulk mineral is difficult with these spectroscopic methods. In contrast, Raman spectroscopy offers clear spectroscopic identification of the different chemical forms of sulfur, and if care is taken to keep the excitation flux low, evaporative loss also can be avoided. Because of these advantages, the technique has already been widely used for the spatially averaged study of surface speciation on sulfide minerals [10–14]. We present here the first spatially resolved chemical maps of elemental sulfur on oxidized pyrite and arsenopyrite surfaces using near-infrared Raman imaging microscopy (NIRIM).

2. Materials and methods

2.1. Mineral preparation

Samples of pyrite (Spain) and arsenopyrite (Mexico) were purchased from Ward's Natural Science. Pyrite crystals were cut parallel to the (0 0 1) natural faces with a diamond wafering saw to produce slabs approximately 4 mm × 4 mm × 2 mm in size with the natural face being one of the larger sides. Irregularly shaped arsenopyrite samples, which do not cleave, were polished to produce exposed faces of approximately 5 mm × 5 mm in order to minimize scattered light that can create a large background signal in Raman spectra. No particular crystallographic orientation was chosen.

The mineral samples were ultrasonically treated in ethanol for 30 min to free any small adhering particles or organic compounds. To remove any oxide layer that may have formed on the mineral surfaces in air, the mineral samples were treated in a 50% solution of HCl for several hours. Previous studies have shown that acid-cleaned pyrite samples exhibit reactivity similar to freshly cleaved samples [23]. Finally, the samples were placed in 10 ml of carbon disulfide for several hours and then rinsed twice with an additional 5 ml. This pretreatment step effectively removes any elemental sulfur already present on the mineral surface and produces a chemically clean starting material for subsequent investigations [24].

2.2. Oxidation experiments

The mineral samples were oxidized in acidic, ferric iron solutions at 42°C for approximately 96 h prior to analysis. The pH and temperature conditions of the experiment were chosen to mimic extreme AMD conditions [25]. Ferric sulfate (Alfa Aesar, reagent grade) was dissolved in sulfuric acid (pH = 1) to produce 500 ppm ferric iron solutions. The reaction flask for each mineral consisted of a

septum-sealed 125 ml Erlenmeyer flask containing 100 ml of the ferric iron solution. Small diameter Tefzel tubing was passed through the septum and each flask was initially purged for several hours with nitrogen (99.999%) in order to saturate the solution prior to the start of the experiment. Control experiments with arsenopyrite in nitrogen-saturated sulfuric acid solutions at pH = 1 (data not shown) revealed negligible extent of reaction over similar time periods.

To begin the oxidation experiment, the mineral samples were added to each flask, and the septa were quickly replaced. After addition of the mineral, the gas flow was maintained at a suitable rate to sustain nitrogen saturation of the reaction solution. Pyrite and arsenopyrite reaction flasks were kept at 42.0 ± 0.1°C for the first 72 h of the experiment. For the final 24 h of the experiment, the reaction solutions were maintained at 42 ± 4°C in septum-sealed flasks, but were not purged with nitrogen. Each mineral sample was imaged within minutes of removal from the reaction flask after being rinsed with deionized water.

2.3. Instrumentation

Raman images of the samples were collected using a NIRIM shown in Fig. 1 [26,27]. This instrument is based on a fiber-bundle image compression (FIC) design, a technique that allows the simultaneous collection of a complete spectral 3D data cube in one read-out of a CCD detector [28,29]. In this FIC based instrument, the light propagates from the sample to the spectrograph through an optical fiber bundle as shown in Fig. 2 [27]. At the collection end, the optical fibers are ordered in a square array where each fiber collects light from a unique spatial point in the sample. At the distal end of the bundle, the optical fibers are ordered in a linear stack that serves as the entrance slit of an imaging spectrograph. The FIC fiber bundle used in the NIRIM consists of 80 fibers (each having a 50 μm core diameter) ordered in a 10×8 square array at the collection end (Fiberoptic Systems). The linear stack is attached to an imaging spectrograph (Kaiser Optical Systems, Holospec f/1.8) and provides 80 Raman spectra per image frame, each with 900 wavelength channels (spanning a 75–1850 cm^{-1} Raman shift

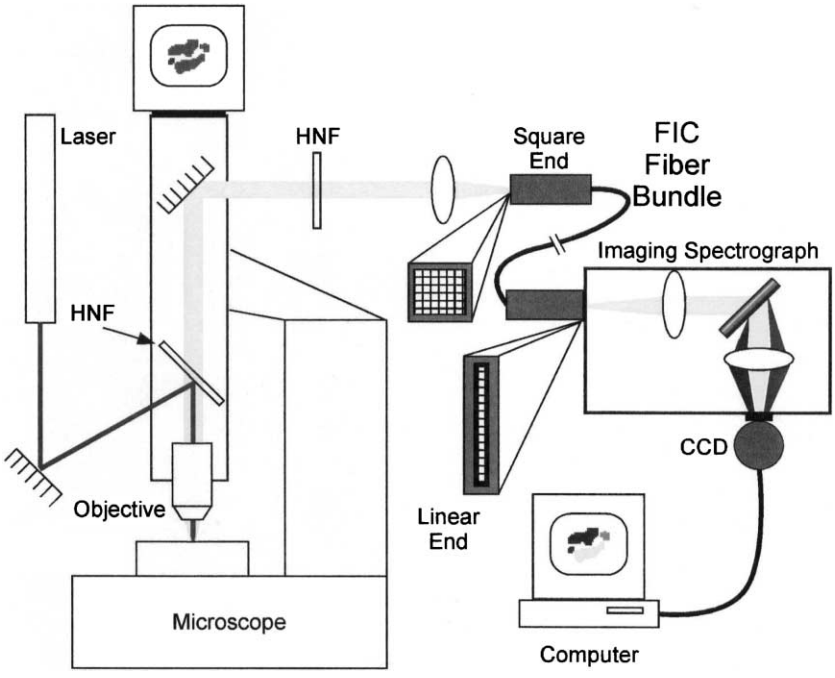

Fig. 1. Schematic diagram of the near-infrared Raman imaging microscope (NIRIM) showing the 785 nm diode laser, microscope, overhead video viewer, FIC fiber bundle, imaging spectrograph, and computer.

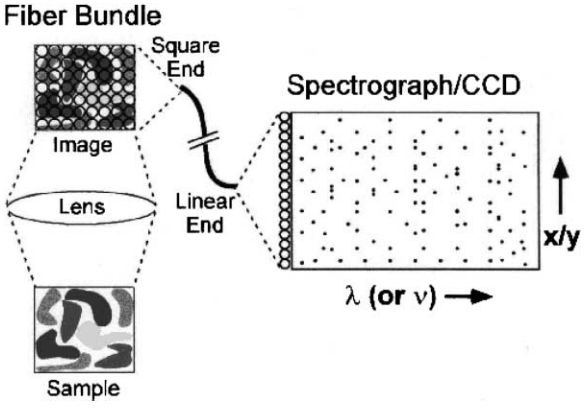

Fig. 2. Graphical representation of the fiber-bundle image compression (FIC) method. The sample is initially imaged onto a square array of fibers where the spatial coordinates are encoded. The fibers are stacked into a linear array at the detection end, and the spectrum within each fiber is dispersed onto a CCD detector.

window with a spectral resolution of 2 cm^{-1}). The sample is imaged onto the fiber bundle by optically coupling the bundle to an Olympus BX-60 microscope. A 40× microscope objective (Olympus IC-40), corresponding to a spatial resolution of 3.0 μm per FIC image pixel, yields a single frame field of view of 30 μm × 24 μm. Images were compiled from 6 × 6 frame raster scans, resulting in a total of 36 frames covering an area equal to 180 μm × 144 μm of the sample surface. This 6 × 6 frame raster scan provides 2880 image pixels, each containing a complete Raman spectrum. The sample is globally illuminated by a 500 mW diode laser (SDL-8630) operating at 785 nm with a total of about 80 mW reaching the sample field of view (or about 1 mW of excitation power per Raman spectrum). All spectra were collected with a single frame integration time of 100 s corresponding to a total integration time of 3600 s per image. Previous studies in our laboratory under comparable conditions (data not shown) have indicated that elemental sulfur is stable at these laser intensities and acquisition times.

3. Results and discussion

3.1. Identification of chemical species using Raman imaging

In order to create a chemical map of the sample surface, the Raman spectrum corresponding to each image pixel must be evaluated for the spectroscopic signature of the chemical species of interest. The top spectrum in each pair of spectra in Fig. 3 is representative raw data obtained from an oxidized pyrite sample. As seen in the first spectrum (Fig. 3a), only two lines corresponding to the phonons from bulk pyrite at 342 and 378 cm^{-1} [30] are evident. In the second spectrum (Fig. 3b), however, additional intense features are observed at approximately 470, 432, 242, 215, and 148 cm^{-1}, which are assigned to elemental sulfur [12]. The sulfur-rich nature of Fe^{3+}-oxidized pyrite surfaces, due to the preferential dissolution of iron at low pH, has been noted in previous studies [10]. Although the elemental sulfur peaks of interest are cleanly resolved from the signal from the bulk mineral, variations in the broad background underlying the Raman features prevent the use of peak heights as a measurement of relative abundance. This background signal, due to scattered light from the roughened mineral surface, fluorescence from impurities within the mineral, or a combination of both, varies considerably from pixel to pixel. The third spectrum (Fig. 3c) illustrates an example of a pyrite spectrum that is dominated by this broad background.

As a means of circumventing the background problem, all spectra were pre-processed using Savitsky–Golay [31–33] second derivative (SGSD). The SGSD

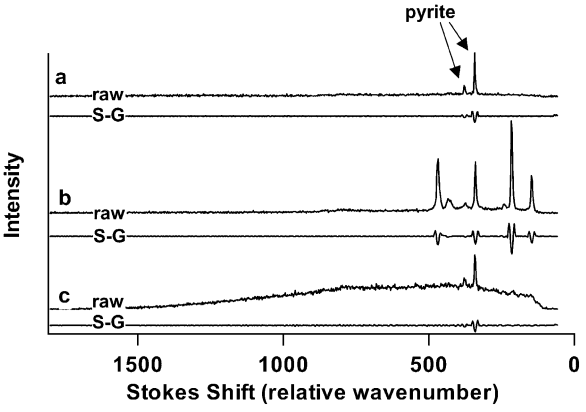

Fig. 3. Representative Raman spectra from an oxidized pyrite surface. Raw spectra (top spectrum in each pair) were the result of 100 s of integration at one pixel with a laser power of ~1 mW. The lines at 342 and 379 cm^{-1} are due to bulk pyrite. Additional lines at 470, 432, 242, 215, and 148 cm^{-1} observed in some spectra are due to the presence of elemental sulfur. The Savitsky–Golay second derivative spectra (bottom one in each pair) were calculated using an 11-point data window.

algorithm may be used to efficiently filter out broad background interference while preserving the chemical information content of the Raman spectral features. The bottom spectrum in each pair in Fig. 3 is the second derivative of the spectrum above it and illustrates the usefulness of SGSD pre-processing in drawing out the desired chemical information. In our system, the best Raman signal enhancement is obtained when the data is processed with an 11-point SGSD window width. In order to extract information about the intensity of elemental sulfur in each spectrum, the minimum in the second derivative spectrum was found for a range of Stokes shifts (189–240 cm^{-1}) that contains one of the large elemental sulfur peaks. Because differences in the broad background of each spectrum are effectively eliminated by the SGSD analysis, determination of the peak value of the second derivative provides a means of gauging differences in Raman signal peak intensity. Images showing the distribution of elemental sulfur on the mineral surface were created by assigning each of the 2880 pixels of the image a grayscale value (0–255) based on the second derivative peak in the elemental sulfur region measured and normalizing this peak to the second derivative of the bulk pyrite peak (minimum value of 315–364 cm^{-1} region).

Fig. 4 presents representative examples of the Raman spectra obtained from oxidized arsenopyrite samples. Raman spectra of arsenopyrite samples, like their pyrite counterparts, reveal clearly resolved elemental sulfur peaks; however, the signal from arsenopyrite itself is not as easily distinguished. The phonon bands of bulk arsenopyrite appear as a series of broad features between 130 and 400 cm^{-1} [13]. As seen in the top spectrum of Fig. 4a, these features are not visible above the noise in many of the spectra. The Raman lines of elemental sulfur, at approximately 470, 432, 242, 215, and 148 cm^{-1} [12], are the dominant features in many of the spectra (Fig. 4b). The relative intensity of the broad background varies considerably between spectra, and, as shown in Fig. 4c, is often a very significant problem.

As in the case of pyrite spectra, SGSD analysis of the arsenopyrite spectra filters out the broad background signal. The bottom spectrum of each pair in Fig. 4 shows the second derivative of the spectrum above it. Chemical information about the presence of elemental sulfur on the mineral surface is retained, while the background noise is efficiently filtered out. As before, the second derivative peak corresponding to one of the elemental sulfur peaks (189–240 cm^{-1}) was used to measure the relative intensity of elemental

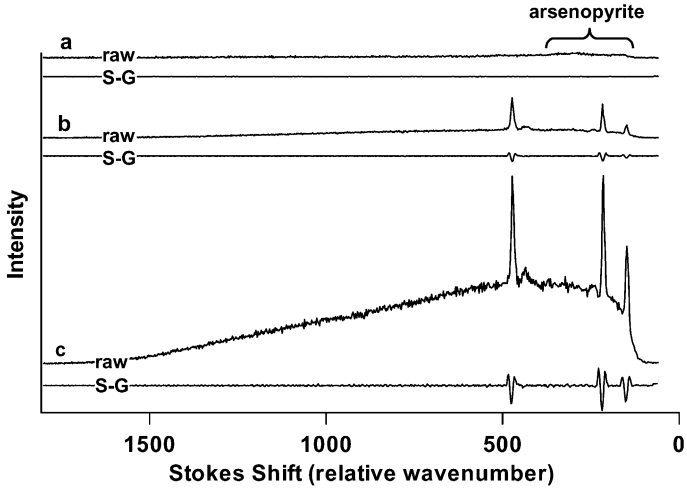

Fig. 4. Representative Raman spectra from an oxidized arsenopyrite surface. Raw spectra (top spectrum in each pair) were the result of 100 s of integration at one pixel with a laser power of ~1 mW. Broad features between 130 and 400 cm^{-1} are due to bulk arsenopyrite. Additional lines at 470, 432, 242, 215, and 148 cm^{-1} observed in some spectra are due to the presence of elemental sulfur. The Savitsky–Golay second derivative spectra (bottom one in each pair) were calculated using an 11-point data window.

sulfur at each image pixel and create a grayscale. Normalization to the underlying arsenopyrite was not possible because the signal from the bulk mineral is often not resolved above the noise and does not contain the cleanly resolved, sharp peaks necessary for a SGSD analysis.

3.2. Application of Raman imaging to pyrite and arsenopyrite surfaces

Quantitative information about the spatial distribution of elemental sulfur can be obtained through statistical analysis of the variations in chemical composition. One useful way of determining the length scale over which the chemical composition varies is through the autocorrelation function. Because the images obtained do not exhibit any directionally specific patterning, a one-dimensional autocorrelation function was sufficient for these analyses

$$g(x) = \int f(x')f(x'+x)\,\mathrm{d}x'$$

In this equation, $f(x')$ is the array of intensity values in the image and x the distance by which the "copy" of the image is shifted in one-dimension before taking the product with the original image. This autocorrelation function, $g(x)$, is maximum when $x = 0$, and falls off with increasing distance x. Fig. 5 illustrates examples of the square root of the autocorrelation function plotted against distance for two different arsenopyrite images. The length scale of appreciable variation reported for each image is the distance at which the square root of the autocorrelation function drops to half of its maximum value. This value represents the root mean square (rms) length scale of the average feature size observed in the image. In the case of the arsenopyrite images used to generate the plots in Fig. 5, the square root of the autocorrelation function drops to half its original value within 8 (Fig. 5a) and 3 pixels (Fig. 5b). This indicates that the effective "length scale" of the chemical variation is approximately 24 and 9 μm, respectively, on these two samples.

Fig. 6a presents the chemical image of elemental sulfur on the natural (0 0 1) crystal face of a pyrite sample that was oxidized in a 500 ppm ferric iron solution at pH = 1 and 42°C for approximately 96 h. The second derivative of the peak at 215 cm^{-1} was

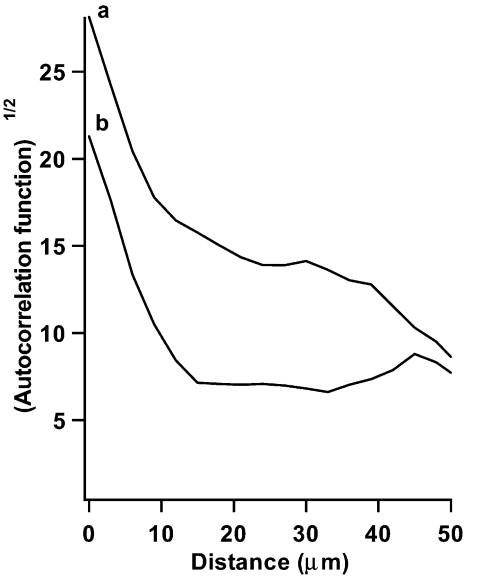

Fig. 5. Square root of the one-dimensional autocorrelation function vs. distance for the arsenopyrite images shown in Fig. 7a (a) and Fig. 7c (b). The square root of the autocorrelation function drops to half its maximum value at distances of (a) 24 and (b) 9 μm.

used to map the variation in elemental sulfur coverage on the pyrite surface. For each pixel in the image, the elemental sulfur value was first normalized to the bulk pyrite peak at 342 cm^{-1}. The resulting image in Fig. 6a corresponds to a 180 μm × 144 μm area of the pyrite surface. The darker regions indicate higher Raman intensities from elemental sulfur. On this particular pyrite sample, the elemental sulfur appears to be spread across the surface in small patches, some of which are of comparable size to or smaller than a single image pixel size (of 3 μm × 3 μm area). The rms length scale of the elemental sulfur features, as determined from a one-dimensional autocorrelation analysis of the image, is 3 pixels, or 9 μm. Between the isolated patches of elemental sulfur, the Raman signal from the bulk pyrite predominates, and little, if any, elemental sulfur is present. These regions are represented by the lighter areas of the image.

Fig. 6b illustrates the chemical image from a second pyrite sample reacted under identical conditions and imaged with the same spectroscopic parameters. In this image, the darker areas, which again correspond to elemental sulfur, are present in larger patches. Large areas of the pyrite surface contain little, if

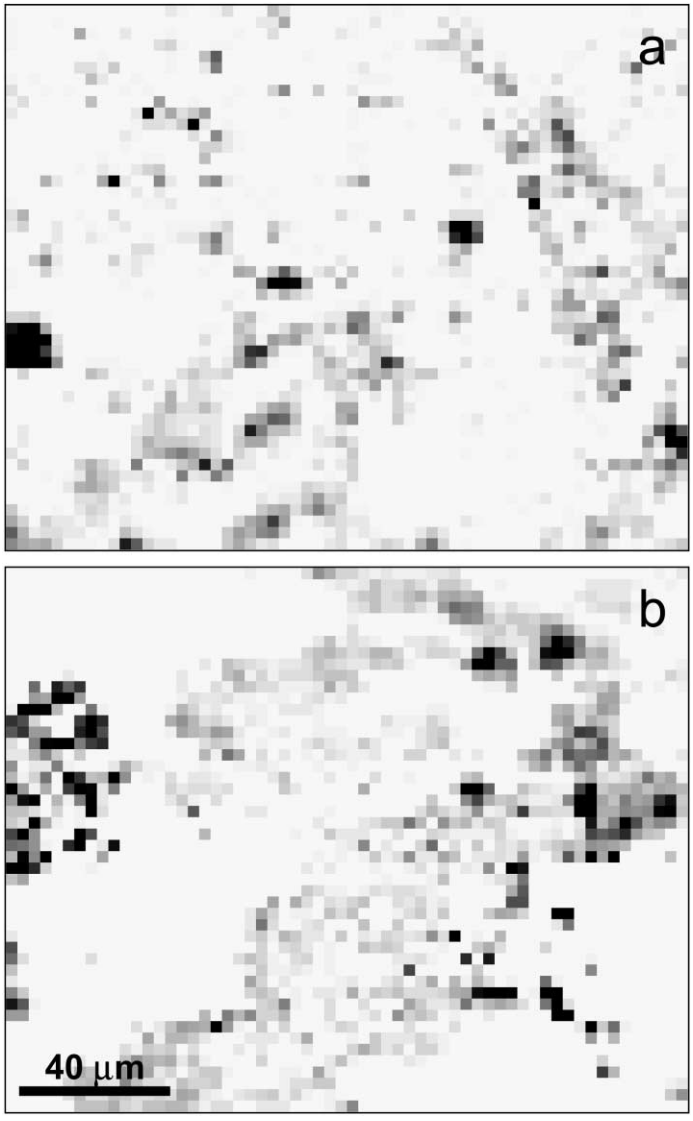

Fig. 6. Chemical images of a 180 μm × 144 μm region of two different oxidized pyrite (0 0 1) surfaces. The relative intensity of the elemental sulfur signal at each point, normalized to the bulk mineral, is represented by the darkness of the pixel. The Raman images are composed of 6 × 6 individual frames that were integrated for 100 s using a 40× objective and a laser power of ∼1 mW per pixel. The approximate pixel-size-limited resolution is 3 μm.

any, elemental sulfur, but the rms length scale of the elemental sulfur features, in this case, is 57 μm. As on the previously examined pyrite sample, the distribution of elemental sulfur is clearly heterogeneous (non-uniform surface coverage) and there is no indication of preferential formation along specific crystallographic directions at this length scale.

Fig. 7a is the resulting chemical image of an arsenopyrite sample that was reacted in a 500 ppm ferric iron solution at pH = 1 and 42°C for 96 h. Each pixel was assigned a value based on the intensity of the elemental sulfur peak at 215 cm^{-1} in the second derivative of the spectrum associated with that pixel. The image corresponds to a 180 μm × 144 μm area of

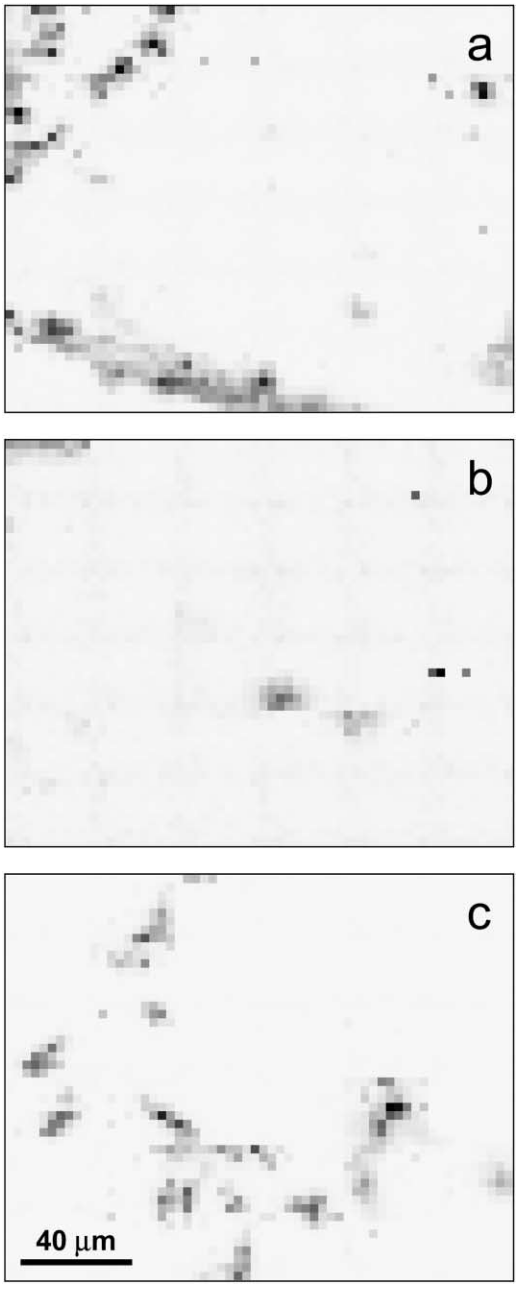

Fig. 7. Chemical images of 180 μm × 144 μm regions of oxidized arsenopyrite surfaces. The images in (b) and (c) were taken at different locations on the same sample. The relative intensity of the elemental sulfur signal at each point is represented by the darkness of each pixel in the image. The Raman images are composed of 6 × 6 individual frames that were integrated for 100 s using a 40× objective and a laser power of ∼1 mW per pixel. The approximate pixel-size-limited resolution is 3 μm.

the polished surface. As seen in Fig. 7a, a large portion of the mineral surface contains elemental sulfur in quantities below the detection limit (see Section 3.4), as represented by the light areas in the chemical image. The darker areas, which contain more elemental sulfur, appear as discrete patches tens of microns across. The rms length scale of the elemental sulfur features, as determined by one-dimensional autocorrelation analysis, is 24 μm.

A second polished arsenopyrite sample was imaged in two different areas and analyzed in the same manner. Fig. 7b illustrates one of these 180 μm × 144 μm areas. Here the light areas of the image contain Raman spectra dominated by the bulk mineral and contain elemental sulfur in quantities below the detection limit. Only several small dark patches of elemental sulfur, with a calculated rms length scale of 18 μm, are seen in the image. In contrast, when the sample was repositioned to illuminate a different region of the polished surface, more elemental sulfur was observed. Fig. 7c shows the image of this second region of the sample. Small elemental sulfur features, with an rms length scale of 9 μm, are scattered across this region of the arsenopyrite surface. As observed in the first region, a large portion of the surface contains no detectable elemental sulfur.

3.3. Binary chemical mapping

As a comparison, an alternative method of data analysis was used to produce binary images from two of the arsenopyrite data sets. The binary analysis method uses the entire spectrum to determine whether or not elemental sulfur is present, in contrast to the previously described grayscale method that uses the maximum intensity in one particular spectral range. For the binary analyses, the last 80 data points in the original spectra were truncated to eliminate artifacts close to the laser wavelength resulting from the holographic notch filter. After SGSD pre-processing, the 3D data cubes then were analyzed using the Multispec spectral image processing software package [34], which facilitates the creation of single- or multiple-channel chemical images using a variety of feature selection, training, and classification algorithms. Binary chemical images were produced using the spectral angle mapping (SAM) classification algorithm [34]. This was done by building a training library consisting

of spectra belonging to elemental sulfur or arsenopyrite. The SAM algorithm then compared each individual image pixel to the different classes in the library, and assigned the pixel to the class it best resembles as defined by the correlation coefficient between the image and library spectra. A large correlation coefficient indicates a strong similarity between the spectra and the classes. In particular, we have set the correlation coefficient threshold to 0.95 (highest value being 1.0), thus making the algorithm very selective in assigning the spectra to the different classes. The assignment of an image pixel to a class is binary; either it belongs to a class or it does not. Consequently, the final processed chemical images of arsenopyrite produced in this way do not contain any intensity information, but do indicate the regions of the sample in which there is a significant amount of the corresponding chemical component.

Fig. 8a and b illustrate the binary images of the same data sets that were used to produce the grayscale images in Fig. 7a and c, respectively. The SAM algorithm classified each pixel as ''arsenopyrite'' or ''arsenopyrite and elemental sulfur'' based on the Raman spectrum associated with that pixel. Although the binary images carry less information about the relative intensity of the elemental sulfur Raman signal, they reveal the same general pattern of elemental sulfur islands on the mineral surface. The similarity of the images obtained by these two analysis methods suggests that the classification algorithm provides information similar to that which could be obtained by setting a threshold value on the grayscale images. This observation confirms that the grayscale map, based on the maximum intensity in one spectral region, can be correlated to the complete Raman spectral signature of elemental sulfur.

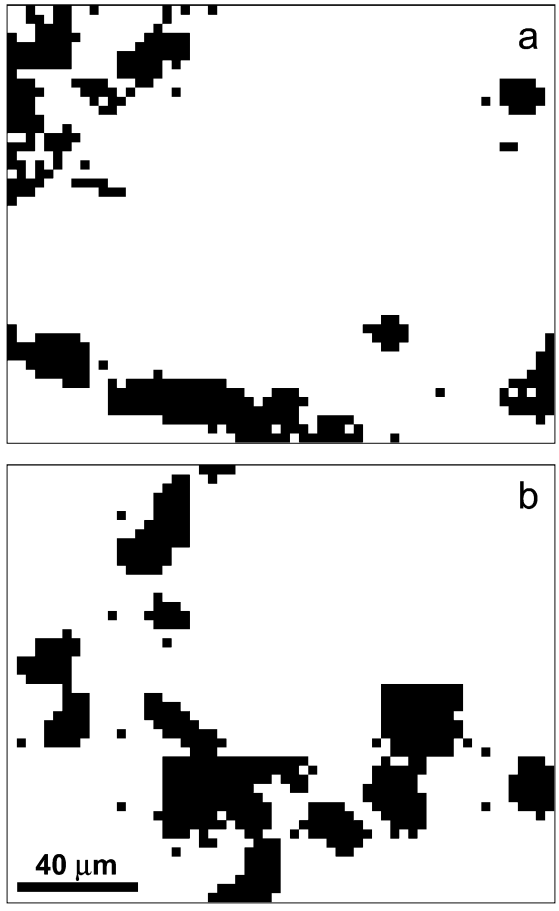

Fig. 8. Binary images (a and b) produced from the same data sets as used in Fig. 7a and c, respectively. The spectrum corresponding to each pixel was classified as either ''arsenopyrite'' or ''arsenopyrite and elemental sulfur'' using the SAM classification algorithm. Dark areas represent elemental sulfur, while the light areas correspond to bare, exposed arsenopyrite.

3.4. Estimation of sulfur layer thickness

In order to obtain a rough, qualitative determination of the thickness of the sulfur layer, the results of these imaging experiments were compared to another study in which the elemental sulfur on arsenopyrite surfaces was quantitatively analyzed. In this quantitative experiment, 0.321 g of crushed arsenopyrite were oxidized by ferric iron under nearly identical conditions to the oxidation of the polished samples imaged in this study. The quantitative analysis, described in detail elsewhere [24], involves extraction of the elemental sulfur from the mineral surface with perchloroethylene and subsequent analysis by high performance liquid chromatography (HPLC). Analysis of the crushed sample, which provides more surface area and hence a measurable quantity of elemental sulfur, found 0.39 mg of elemental sulfur.

The surface area of the 75–150 μm sieve fraction of the crushed arsenopyrite sample was measured as 0.082 m^2/g by Krypton BET surface area analysis (Porous Materials, Inc., Ithaca, NY). Thus, the total surface area of the reacted sample was 260 cm^2. Based on the three NIRIM images of arsenopyrite samples,

the average percent of the surface that is covered by elemental sulfur appears to be approximately 10%. Applying this percentage to the crushed mineral sample for which the amount of elemental sulfur was determined, the surface density of the individual sulfur deposits can be estimated as 10^{-5} g/cm^2. Given that the density of elemental sulfur is 2 g/cm^3 [35], this analysis indicates that the average thickness of the individual elemental sulfur deposits at the mineral surface is on the order of a hundred nanometers. Although this calculation provides a very crude estimation of the thickness of the elemental sulfur deposits, it does suggest that the thickness of the elemental sulfur observed in the NIRIM images is probably tens to hundreds of molecular layers. Additionally, because the average signal-to-noise ratio of the elemental sulfur signal is on the order of 100, the detection limit of these Raman imaging experiments can be estimated as a few molecular layers of elemental sulfur. Due to the inherently low yield of the Raman scattering process, limits imposed on the laser intensity by heating and sample damage concerns, and the already high efficiency of the collection and detection system, this may represent the best sensitivity that can be achieved readily in Raman imaging.

3.5. Implications of elemental sulfur distribution on pyrite and arsenopyrite surfaces

The heterogeneous distribution of elemental sulfur has important implications for the kinetics of sulfide mineral dissolution. Several studies have suggested that the accumulation of elemental sulfur on sulfide minerals passivates the surface to further oxidation by preventing the passage of oxidants to the surface [36–39]. In contrast, other studies have demonstrated that removal of the elemental sulfur layer at the surface produces no measurable change in the rate of dissolution of the underlying mineral at low concentrations of ferrous iron [13,40]. The findings reported here help to clarify these apparent contradictions. NIRIM chemical mapping has shown that the distribution of elemental sulfur on oxidized pyrite and arsenopyrite surfaces is extremely heterogeneous. After oxidation for a period of days, elemental sulfur appears as discrete patches, dispersed randomly across the sample surface. Different regions of the same sample can display drastically dissimilar patterns of elemental sulfur coverage. The length scale of appreciable variation in elemental sulfur coverage appears to be on the order of tens of microns. Additionally, large areas of the mineral surface, on similar length scales, contain quantities of elemental sulfur below the detection limit. The extremely heterogeneous nature of the sulfide mineral surface suggests that, at least on the time scale of laboratory experiments, elemental sulfur does not form a continuous, passivating layer at the mineral surface. Although previous studies have shown that small quantities of adsorbates can affect the rate of dissolution of pyrite by blocking active sites at the mineral surface [41,42], the results of the previous kinetic experiments [13,40] suggest that the sites of elemental sulfur nucleation most likely do not coincide with the oxidation active sites.

At the present time, it is not clear why elemental sulfur is found in specific, localized patches at the mineral surface. Sulfide minerals contain dislocations and inclusions that may provide preferential sites for nucleation of elemental sulfur. Further investigation is needed to understand if localized sites do indeed direct the mechanism of formation or nucleation of elemental sulfur, and whether elemental sulfur is localized to areas of active oxidation. Information regarding the spatial distribution of elemental sulfur on the mineral surface certainly is the first step toward creating a more complete model of sulfide mineral oxidation.

4. Conclusions

Our studies of elemental sulfur on sulfide mineral surfaces illustrate the type of spatially resolved information that can be gleaned from chemical mapping. Raman imaging, combined with quantitative spatial analysis of the images, is a useful analytical method for understanding heterogeneous geochemical processes. The spatial distribution of surface products can provide valuable clues about the kinetics and mechanism of a wide range of complex geochemical systems and environmental problems.

Acknowledgements

This work was supported by grants from the Environmental Protection Agency (R 826189), the National

Science Foundation (CHE 9807598), and the Office of Naval Research (ONR N00014-99-1-0155). The authors also wish to acknowledge Dr. Jillian Banfield for many helpful discussions.

References

[1] V.P. Evangelou, Y.L. Zhang, Crit. Rev. Environ. Sci. Technol. 25 (1995) 141.
[2] R.T. Lowson, Chem. Rev. 82 (1982) 461.
[3] D.K. Nordstrom, in: J.A. Kittrick, D.S. Fanning, L.R. Hossner (Eds.), Acid Sulfate Weathering, Soil Science Society of America, Madison, WI, 1982, p. 37.
[4] D.K. Nordstrom, G. Southam, in: J.F. Banfield, K.H. Nealson, (Eds.), Geomicrobiology: Interactions Between Microbes and Minerals, Mineralogical Society of America, Washington, DC, 1997, p. 361.
[5] D.K. Nordstrom, C.N. Alpers, in: G.S. Plumlee, M.J. Logsdon (Eds.), Environmental Geochemistry of Mineral Deposits, Society of Economic Geologists, Littleton, CO, 1999, p. 133.
[6] M.A. McKibben, H.L. Barnes, Geochim. Cosmochim. Acta 50 (1986) 1509.
[7] C.O. Moses, D.K. Nordstrom, J.S. Herman, A.L. Mills, Geochim. Cosmochim. Acta 51 (1987) 1561.
[8] P.C. Singer, W. Stumm, Science 167 (1970) 1121.
[9] G.W. Luther III, Geochim. Cosmochim. Acta 51 (1987) 3193.
[10] K. Sasaki, M. Tsunekawa, T. Ohtsuka, H. Konno, Geochim. Cosmochim. Acta 59 (1995) 3155.
[11] K. Sasaki, Can. Miner. 35 (1997) 999.
[12] J.R. Mycroft, G.M. Bancroft, N.S. McIntyre, J.W. Lorimer, I.R. Hill, J. Electroanal. Chem. 292 (1990) 139.
[13] M.M. McGuire, K.J. Edwards, J.F. Banfield, R.J. Hamers, Geochim. Cosmochim. Acta 65 (2001) 57.
[14] S.B. Turcotte, R.E. Benner, A.M. Riley, J. Li, M.E. Wadsworth, D.M. Bodily, J. Electroanal. Chem. 347 (1993) 195.
[15] V. Toniazzo, C. Mustin, J.M. Portal, B. Humbert, R. Benoit, R. Erre, Appl. Surf. Sci. 143 (1999) 229.
[16] J.M. Guevremont, D.R. Strongin, M.A.A. Schoonen, Surf. Sci. 391 (1997) 109.
[17] J.M. Guevremont, D.R. Strongin, M.A.A. Schoonen, Am. Miner. 83 (1998) 1246.
[18] J.M. Guevremont, J. Bebie, A.R. Elsetinow, D.R. Strongin, M.A.A. Schoonen, Environ. Sci. Technol. 32 (1998) 3743.
[19] C.M. Eggleston, M.F. Hochella Jr., Am. Miner. 77 (1992) 221.
[20] C.M. Eggleston, J.-J. Ehrhardt, W. Stumm, Am. Mineral. 81 (1996) 1036.
[21] K.M. Rosso, U. Becker, M.F. Hochella Jr., Am. Miner. 84 (1999) 1549.
[22] A.N. Buckley, I.C. Hamilton, R. Woods, in: K.S.E. Forssberg (Ed.), Flotation of Sulfide Minerals, Elsevier, Amsterdam, 1985, p. 41.
[23] A.R. Elsetinow, J.M. Guevremont, D.R. Strongin, M.A.A. Schoonen, M. Strongin, Am. Miner. 85 (2000) 623.
[24] M.M. McGuire, R.J. Hamers, Environ. Sci. Technol. 34 (2000) 4651.
[25] K.J. Edwards, B.M. Goebel, T.M. Rodgers, M.O. Schrenk, T.M. Gihring, M.M. Cardona, B. Hu, M.M. McGuire, R.J. Hamers, N.R. Pace, J.F. Banfield, Geomicrobiol. J. 16 (1999) 155.
[26] A.D. Gift, J. Ma, K.S. Haber, B.L. McClain, D. Ben-Amotz, J. Raman Spectrosc. 30 (1999) 757.
[27] B.L. McClain, H.G. Hedderich, A.D. Gift, D. Zhang, K.N. Jallad, K.S. Haber, J. Ma, D. Ben-Amotz, Spectroscopy 15 (2000) 28.
[28] J. Ma, D. Ben-Amotz, Appl. Spectrosc. 51 (1997) 1845.
[29] B.L. McClain, J. Ma, D. Ben-Amotz, Appl. Spectrosc. 53 (1999) 1118.
[30] S. Ushioda, Solid State Commun. 10 (1972) 307.
[31] A. Savitsky, M.J.E. Golay, Anal. Chem. 36 (1964) 1627.
[32] D. Zhang, D. Ben-Amotz, Appl. Spectrosc. 54 (2000) 1379.
[33] J. Steinier, Y. Termonia, J. Deltour, Anal. Chem. 44 (1972) 1906.
[34] L. Biehl, D. Langrebe, MultiSpec — A Tool for Multispectral Image Data Analysis, Pecora 13, Sioux Falls, SD, 1996.
[35] D.R. Lide (Ed.), CRC Handbook of Chemistry and Physics, 73rd Edition, CRC Press, Boca Raton, FL, 1992.
[36] G. Curutchet, P. Tedesco, E. Donati, Biotechnol. Lett. 18 (1996) 1471.
[37] M. Dopson, E.B. Lindstrom, Appl. Environ. Microbiol. 65 (1999) 36.
[38] O. Garcia Jr., J.M. Bigham, O.H. Tuovinen, Can. J. Microbiol. 41 (1995) 578.
[39] O. Garcia Jr., J.M. Bigham, O.H. Tuovinen, Can. J. Microbiol. 41 (1995) 508.
[40] T.A. Fowler, F.K. Crundwell, Appl. Environ. Microbiol. 65 (1999) 5285.
[41] K. Sasaki, M. Tsunekawa, S. Tanaka, H. Konno, Colloid Surf. A 119 (1996) 241.
[42] B.C. Bostick, S. Fendorf, B.T. Bowie, P.R. Griffiths, Environ. Sci. Technol. 34 (2000) 1494.